SIAM J. APPL. MATH.
Vol. 66, No. 4, pp. 1339–1365

MULTIPARAMETRIC BIFURCATION ANALYSIS OF A BASIC TWO-STAGE POPULATION MODEL*

S. M. BAER†, B. W. KOOI‡, YU. A. KUZNETSOV§, AND H. R. THIEME¶

Abstract. In this paper we investigate long-term dynamics of the most basic model for stage-structured populations, in which the per capita transition from the juvenile into the adult class is density dependent. The model is represented by an autonomous system of two nonlinear differential equations with four parameters for a single population. We find that the interaction of intra-adult competition and intra-juvenile competition gives rise to multiple attractors, one of which can be oscillatory. A detailed numerical study reveals a rich bifurcation structure for this two-dimensional system, originating from a degenerate Bogdanov–Takens (BT) bifurcation point when one parameter is kept constant. Depending on the value of this fixed parameter, the corresponding triple critical equilibrium has either an elliptic sector or it is a topological focus, which is demonstrated by the numerical normal form analysis. It is shown that the canonical unfolding of the codimension-three BT point reveals the underlying dynamics of the model. Certain new features of this unfolding in the elliptic case, which are important in applications but have been overlooked in available theoretical studies, are established. Various three-, two-, and one-parameter bifurcation diagrams of the model are presented and interpreted in biological terms.

Key words. bifurcation analysis, Bogdanov–Takens codimension-three point, elliptic sector, homoclinic orbits to saddle, saddle-node, and neutral saddle, two-stage population model

AMS subject classifications. 34C23, 92D25, 37G05

DOI. 10.1137/050627757

1. Introduction.

Population growth models that include age, stage or body size structure often predict complex population dynamics. The models are rather sophisticated, involving partial or functional differential equations, difference equations, or integral equations [3, 6, 7, 35]. In this paper, we investigate a simple-stage structured model governed by a two-dimensional system of time-autonomous ordinary differential equations. The equations represent the juvenile and adult stage, respectively. We show that this reduced but biologically-based model predicts, qualitatively, complex population dynamics. Of course, the complexity is restricted by the Poincaré–Bendixson theory. Earlier work addressing competition between age stages [21] found that periodic orbits can surround a unique interior equilibrium. Here we show that multiple equilibria are possible, both stable and unstable periodic orbits can exist and even coexist, and homoclinic orbits can occur through the interaction of periodic orbits and multiple equilibria.

The best-known two-dimensional ODE system in population biology is the Lotka–Volterra predator/prey model where the dynamic behavior is simple but structurally

*Received by the editors March 26, 2005; accepted for publication (in revised form) November 15, 2005; published electronically April 21, 2006.
http://www.siam.org/journals/siap/66-4/62775.html

†Department of Mathematics and Statistics, Arizona State University, Tempe, AZ 85287 (baer@math.la.asu.edu).

‡Department of Theoretical Biology, Vrije Universiteit, de Boelelaan 1087, 1081 HV Amsterdam, the Netherlands (kooi@bio.vu.nl).

§Mathematical Institute, Utrecht Universiteit, Budapestlaan 6, 3584 CD Utrecht, the Netherlands (kuznetsov@math.uu.nl).

¶Department of Mathematics and Statistics, Arizona State University, Tempe, AZ 85287 (thieme@math.la.asu.edu). This author was partially supported by NSF grants DMS-9706787 and 0314529.

unstable. In an extension of this model, called the Rosenzweig–MacArthur model, the trophic interaction is described by a hyperbolic functional response instead of a linear functional response. If a carrying capacity for the prey is added, stable oscillations can occur, but no more complex dynamics. An extension of the Rosenzweig–MacArthur model was proposed and studied in [1], where the per capita mortality rate of the predators is replaced by a density-dependent mortality rate, and in [40] where the Holling type II functional response is replaced by a nonmonotonic Holling type IV functional response for the predator-prey interaction. These planar systems show rich asymptotic dynamic behavior including global bifurcations and a variety of codimension-two points originating from codimension-three bifurcation points.

We deal with a model for one population with two stages introduced in [21] and further studied in [34, Chapter 11]. The life history of the individuals comprises a juvenile and an adult stage. The population state is the number of juveniles and adults. Juveniles and adults die, while adults reproduce. The transition rate between the two stages, together with the per capita mortality and reproduction rates, form the parameters of the two first-order ordinary differential equations (ODEs) which specify the time derivative of the population state.

We use bifurcation analysis to study the dependence of the long-term dynamic behavior of this system on parameter variation. See [16, 36, 32, 22] for an introduction to bifurcation analysis and [1] for applications to ecosystem models. The structural stability is studied with respect to so-called free or bifurcation parameters. Parameter values at which the asymptotic dynamics change are called bifurcation points; for example, a Hopf bifurcation point represents a transition between constant and time-periodic solutions. Starting at this point one can vary two parameters simultaneously. This is sometimes called a two-parameter bifurcation study. The resulting bifurcation curves separate regions in the two-dimensional parameter space, which differ in qualitative asymptotic behavior. At so-called codimension-two points three or more parameter regions come together. In other words, different types of bifurcation points can originate from or terminate at these points, making these points useful for starting a numerical bifurcation analysis. Codimension-two points can be followed by varying three parameters simultaneously, and so on.

Our stage-structured population model is a two-dimensional system with four parameters. When one parameter is fixed, a degenerate Bogdanov–Takens bifurcation (BT point for short) with a triple critical equilibrium is found. Different types of such degenerate BT points are studied in detail in [2, 12], where three categories of topological types are distinguished: the saddle, the focus, and the elliptic case. We will derive a normal form with terms up to and including fourth order for the codimension-three BT point by using a time reparameterization combined with a smooth transformation that also includes fourth-order terms. This analysis reveals that the elliptic or focus case applies for the two-stage population model depending on the value of the fixed parameter. When this parameter is varied a transition from elliptic to focus codimension-three BT bifurcation is found.

The truncated normal form of the codimension-three BT point in the elliptic case is embedded into an appropriate three-parameter family, and we study its unfolding by performing a numerical bifurcation analysis for the neighborhood of the origin in that three-dimensional parameter space. In the three-dimensional parameter space, two branches of codimension-two BT curves emanate from the codimension-three point. These curves form the intersection of saddle-node and Hopf bifurcation planes. Furthermore, codimension-two Bautin bifurcations as well as codimension-two homoclinic orbits to neutral saddles originate from the codimension-three BT point.

In two-parameter space, codimension-one homoclinic bifurcation curves can originate from BT points. Both saddle, saddle-node and neutral saddle homoclinic orbit bifurcations actually occur. The analysis reveals unexpected similarities between the elliptic and the focus cases, which have been overlooked in earlier theoretical studies.

The normal form analysis results are used to interpret those of the numerical bifurcation analysis study of the full planar two-stage population model and consequently also those reported in [34, Chapter 11].

2. The two-stage population model. The model is introduced in [21] and further motivated in [34, Chapter 11]. The population is split into juveniles (larvae, e.g.) and adults, the numbers of which are denoted by $L(t)$ and $A(t)$, respectively. The system has the form

$$\frac{dL}{dt} = \beta(L,A)A - \mu(L,A)L - f(L,A)L\,, \tag{2.1a}$$

$$\frac{dA}{dt} = f(L,A)L - \alpha(L,A)A\,, \tag{2.1b}$$

where β is the per capita reproduction rate of an average adult individual, μ is the per capita mortality rate of an average juvenile individual (α for the adults) and f the per capita transition rate from the juvenile into the adult stage. In general, these rates can depend on both the densities of juveniles and adults.

Under realistic additional assumptions, all trajectories converge to an equilibrium (not necessarily the same) if $\frac{\partial}{\partial L}[f(L,A)L] \geq 0$ for all $L, A > 0$ [34, Thm. 11.6]. (See [21] for a convergence result under different assumptions.) So there are no complex dynamics if the transition from the juvenile to the adult stage is only weakly affected by intra-juvenile competition. However, we show in this paper that complex behavior may indeed occur if there is both a strong influence on the per capita transition rate by intra-juvenile competition and a strong effect on the per capita birth rate by intra-adult competition. We restrict our consideration to pure intrastage competition, i.e., there is no competition between juveniles and adults. So the juvenile per capita mortality rate depends on the number of juveniles, i.e., $\mu(L)$, and the adult per capita mortality rate $\alpha(A)$ and reproduction rate $\beta(A)$ depend only on the number of adults A. This may occur when juveniles and adults have different habitats. For simplicity, the per capita mortality rates for both juveniles and adults are taken as constants. Time is scaled such that $\alpha = 1$; this means that one time unit equals the expectation of adult life. For convenience we divide the other rates β, μ and f by α, but we do not introduce new variables. As in [21], a Ricker-type function is chosen for the stage transition rate,

$$f(L) = \frac{\mu}{m}e^{-L}. \tag{2.2}$$

The reproduction rate $\beta(A)$ is chosen as

$$\beta(A) = g\big(\frac{m}{\mu}A\big). \tag{2.3}$$

To interpret the parameter m, we consider the expression for the probability of surviving the juvenile stage to become an adult in the absence of competition ($L = 0$):

$$p = \frac{f(0)}{\mu + f(0)} = \frac{1}{1+m}, \tag{2.4}$$

where $f(0)$ is evaluated using (2.2). The numerator $f(0)$ is the per capita transition rate from the juvenile and the adult stage (without competition) and the denominator $\mu + f(0)$ is the total rate at which juveniles leave their stage. For $m = 0$ all juveniles survive to adults, for $m = 1$ half survive, and as $m \to \infty$ the probability of surviving approaches zero.

After introducing the scaled number of adults y as

$$y = \frac{m}{\mu} A, \tag{2.5}$$

the stage-structured population model becomes

$$\frac{dL}{dt} = \frac{\mu}{m}\big[g(y)y - mL - Le^{-L}\big], \tag{2.6a}$$

$$\frac{dy}{dt} = Le^{-L} - y. \tag{2.6b}$$

At equilibrium, (2.6b) gives a fixed relationship between y^* and L^* which is independent of all parameters. Note from (2.6a) that these values are independent of the parameter μ. We assume that the birth rate $g(y)$ is also of Ricker-type:

$$g(y) = e^{(1/b)(a-y)}. \tag{2.7}$$

When not varied, the model parameters have the following reference values $a = 0.43, b = 2.2, m = 0.01$, while $0 \le \mu \le 1.0$.

3. Organizing centers. This section is partially based on [34, section 11.9]. The system (2.6) has been scaled in such a way that the equilibria do not depend on the parameter μ. The origin $(L = 0, y = 0)$ is always an equilibrium.

The parameter m can be expressed as a function of the L-component of the interior equilibria, L^*,

$$m = \big[g(L^*e^{-L^*}) - 1\big]e^{-L^*} =: M(L^*). \tag{3.1}$$

The value

$$m_0 = M(0) = g(0) - 1 = e^{a/b} - 1 \tag{3.2}$$

is the threshold value for the existence of interior equilibria and the stability of the origin. The Jacobian of system (2.6) evaluated at the origin reads

$$\begin{pmatrix} -\frac{\mu}{m}(m+1) & \frac{\mu}{m}g(0) \\ 1 & -1 \end{pmatrix}. \tag{3.3}$$

The determinant of this Jacobian matrix switches its sign at m_0. Hence, m_0 marks a transcritical bifurcation. If $m \ge m_0$, the origin is the only equilibrium and it attracts all solutions starting in the biologically relevant nonnegative quadrant. We therefore restrict our investigation to $m \in (0, m_0)$. Then the origin is a saddle with one part of its unstable manifold lying in the positive quadrant. Moreover the origin is a strong repeller and not part of ω-limit sets of solutions starting in the nonnegative quadrant, except at the origin itself. Further, there exists at least one interior equilibrium.

Whatever the choice of the positive parameters a and b, the function M is strictly decreasing for small $L^* > 0$ and large $L^* > 0$. It can also be shown that the equation $M(L^*) = m$ has at most three interior solutions. This implies that, depending on the

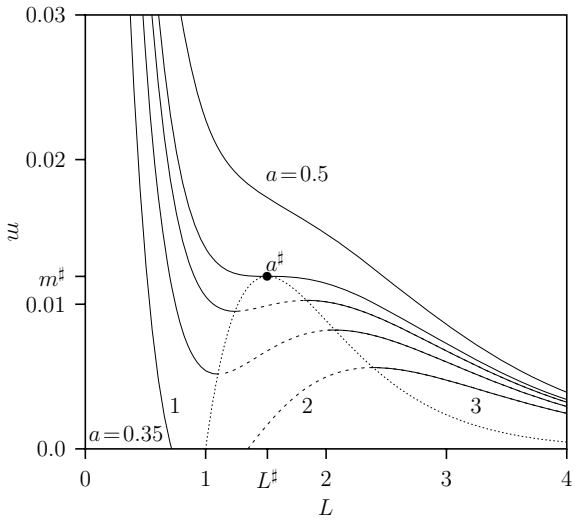

FIG. 3.1. *Graph of the function M for $b = 2.2$ and various values of a. From right to left: $a = 0.5$, $a = a^\sharp = 0.4492276697$, $a = 0.43$, $a = 0.4$, $a = 0.35$. The bullet gives the simultaneous point of inflection and critical point for $a = a^\sharp$. The dotted line connects the critical points where a is varied. The numbers label the branches where equilibrium E_i occurs at branch $i = 1, 2, 3$.*

choice of a and b, M is either strictly decreasing on $[0, \infty)$ or that there are numbers $L_2, L_1 > 0$ such that M is strictly decreasing on $[0, L_1]$ and $[L_2, \infty)$ and strictly increasing on $[L_1, L_2]$. When the transition occurs, the three positive equilibria merge into one *triple* equilibrium, and we have a unique $L^* > 0$ such that $M'(L^*) = 0 = M''(L^*) = 0$. If we fix $b > 0$, we can use this relation to determine the value of a at which the transition occurs, say $a^\sharp$. Then, M is strictly decreasing for $a > a^\sharp$ and has changing monotonicity behavior for $a < a^\sharp$. The value of L at the corresponding equilibrium $L^\sharp = L^*$, which together with (3.1) finally gives $m^\sharp = M(L^*)$ and $y^\sharp = y^* = L^* e^{-L^*}$.

Figure 3.1 shows the graph of the function M for $b = 2.2$ and various values of a. The dotted curve marks points where $M'(L^*) = 0$ when a is varied. This curve cuts the horizontal axis $m = 0 = M(L^*)$ at $L^* = 1$, where $a = a_\sharp = 0.3679$.

For the fixed choice of $a_\sharp < a < a^\sharp$ and $b > 0$, M changes its monotonicity; moreover M is strictly positive on $[0, \infty)$. Let

$$m_0 = M(0) = g(0) - 1, \qquad m_1 = M(L_1), \qquad m_2 = M(L_2). \tag{3.4}$$

The critical points L_1 and L_2 can be determined as the solutions of $M'(L) = 0$ and one finds $m_0 > m_2 > m_1$.

We have the following cases depending on m:

$m = m_1$: There are exactly two interior equilibria and their L-components satisfy $L_1^* = L_1$ and $L_2^\diamond := L_2^* > L_2$.

$m = m_2$: There are exactly two interior equilibria, and their L-components satisfy $L_1^\diamond := L_1^* \in (0, L_1)$ and $L_2^* = L_2$.

Then,

$m \geq m_0$: There is no interior equilibrium.

$m \in (m_2, m_0)$: There is exactly one interior equilibrium and its L-component satisfies $L^* \in (0, L_1^\diamond)$.

$m \in (m_1, m_2)$: There are exactly three interior equilibria and their L-components satisfy $L_1^* \in (L_1^\diamond, L_1)$, $L_2^* \in (L_1, L_2)$, $L_3^* \in (L_2, L_2^\diamond)$.

$m \in (0, m_1)$: There is exactly one interior equilibrium and its L-component satisfies $L^* > L_2^\diamond$.

$m = 0$: There is exactly one interior equilibrium $L^* = 1$.

One can show (see [34, page 173]) that the determinant of the Jacobian matrix of the system (2.6), with $y = Le^{-L}$, has the opposite sign of the derivative of M. Hence, every interior equilibrium with $L^* = L_1$ or $L^* = L_2$ has at least one eigenvalue 0. As we have seen, such equilibria occur if and only if $m = m_1$ or $m = m_2$. It can also be shown (see [34, page 172]) that the trace of the Jacobian matrix evaluated at an interior equilibrium is a linear function of μ. The trace switches its sign from negative to positive at

$$\mu = \phi(L^*) := \frac{g(y^*) - 1}{L^* - g(y^*)}, \qquad y^* = L^* e^{-L^*}. \tag{3.5}$$

At $a = a^\sharp$ we have $L^* = L_1 = L_2 = L^\sharp$ and $m = m_1 = m_2 = m^\sharp$, see Figure 3.1. At this point the determinant and the trace of the Jacobian matrix evaluated at the equilibrium $(L^\sharp, y^\sharp)$ are zero. Therefore, for fixed $b > 0$ and $\mu = \mu^\sharp, m = m^\sharp$, and $a = a^\sharp$, we have a BT point. Moreover, the equilibrium is triple at this point; thus a degenerate BT point occurs.

For $b = 2.2$, we have

$$L^\sharp = 1.513180178,\ y^\sharp = 0.33321523 \tag{3.6}$$

and

$$\mu^\sharp = 0.01179614,\ m^\sharp = 0.01192386945,\ a^\sharp = 0.4492276697. \tag{3.7}$$

4. Normal form analysis. In this section we perform a normal form analysis of the degenerate BT point and study its canonical unfolding.

4.1. Critical normal form. First, we write system (2.1) for fixed $b > 0$ at the critical parameter values (3.7) in a coordinate system where the equilibrium with the coordinates (3.6) is shifted to the origin of the phase plane by the transformation

$$\mathbf{x} = \begin{pmatrix} x_1 \\ x_2 \end{pmatrix} = \begin{pmatrix} L - L^\sharp \\ y - y^\sharp \end{pmatrix}. \tag{4.1}$$

The transformed planar system becomes

$$\dot{\mathbf{x}} = \mathbf{J}\mathbf{x} + \mathbf{F}(\mathbf{x}), \tag{4.2}$$

where $\mathbf{J}$ is the Jacobian matrix evaluated at the equilibrium and $\mathbf{F}(\mathbf{x}) = O(\|\mathbf{x}\|^2)$.

Next we use a similarity transformation to put the linear part in the Jordan canonical form. First we calculate two vectors $\mathbf{u}, \mathbf{v} \in \mathbb{R}^2$ such that

$$\mathbf{J}^2\mathbf{v} = 0, \quad \mathbf{J}\mathbf{v} = \mathbf{u}, \quad \|\mathbf{u}\| = 1, \tag{4.3}$$

where the vector norm is defined by $\|\mathbf{u}\|^2 = \langle \mathbf{u}, \mathbf{u} \rangle$ and $\langle \mathbf{u}, \mathbf{v} \rangle$ stands for the standard inner product in $\mathbb{R}^2$: $u_1 v_1 + u_2 v_2$. These two vectors (the eigenvector $\mathbf{u}$ and the generalized eigenvector $\mathbf{v}$), are linearly independent and form a basis in the plane. Notice that $\mathbf{v}$ is the eigenvector belonging to the zero eigenvalue of the matrix $\mathbf{J}^2$

($\mathbf{J}$ is nilpotent of index 2, that is, $\mathbf{J}^2\mathbf{v} = \mathbf{0}$ but $\mathbf{J}\mathbf{v} \neq \mathbf{0}$). One can calculate $\mathbf{v}$ as an eigenvector associated with the zero eigenvalue of the squared Jacobian matrix evaluated at the equilibrium point.

The similarity transformation is now defined by

$$\mathbf{x} = \mathbf{U}\mathbf{y}, \tag{4.4}$$

where $\mathbf{U}$ denotes the matrix the columns of which are formed by a normalized eigenvector and a generalized eigenvector. The matrix $\mathbf{U}$ is invertible, since the vectors $\mathbf{u}$ and $\mathbf{v}$ are linearly independent, and we can write

$$\mathbf{y} = \mathbf{U}^{-1}\mathbf{x}. \tag{4.5}$$

Then

$$\mathbf{U}^{-1}\mathbf{J}\mathbf{U} = \mathbf{J}_0 = \begin{pmatrix} 0 & 1 \\ 0 & 0 \end{pmatrix} \tag{4.6}$$

and

$$\dot{\mathbf{y}} = \mathbf{J}_0\mathbf{y} + \mathbf{U}^{-1}\mathbf{F}(\mathbf{U}\mathbf{y}). \tag{4.7}$$

Taylor series expansion of the right-hand side of (4.7) at the equilibrium $\mathbf{y} = \mathbf{0}$ gives

$$\begin{aligned} \frac{dy_1}{dt} &= y_2 + \frac{1}{2}a_{20}y_1^2 + a_{11}y_1y_2 + \frac{1}{2}a_{02}y_2^2 \\ &\quad + \frac{1}{6}a_{30}y_1^3 + \frac{1}{2}a_{21}y_1^2y_2 + \frac{1}{2}a_{12}y_1y_2^2 + \frac{1}{6}a_{03}y_2^3 \\ &\quad + \frac{1}{24}a_{40}y_1^4 + \frac{1}{6}a_{31}y_1^3y_2 + \frac{1}{4}a_{22}y_1^2y_2^2 + \frac{1}{6}a_{13}y_1y_2^3 + \frac{1}{24}a_{04}y_2^4 + O(\|\mathbf{y}\|^5), \end{aligned} \tag{4.8a}$$

$$\begin{aligned} \frac{dy_2}{dt} &= \frac{1}{2}b_{20}y_1^2 + b_{11}y_1y_2 + \frac{1}{2}b_{02}y_2^2 \\ &\quad + \frac{1}{6}b_{30}y_1^3 + \frac{1}{2}b_{21}y_1^2y_2 + \frac{1}{2}b_{12}y_1y_2^2 + \frac{1}{6}b_{03}y_2^3 \\ &\quad + \frac{1}{24}b_{40}y_1^4 + \frac{1}{6}b_{31}y_1^3y_2 + \frac{1}{4}b_{22}y_1^2y_2^2 + \frac{1}{6}b_{13}y_1y_2^3 + \frac{1}{24}b_{04}y_2^4 + O(\|\mathbf{y}\|^5). \end{aligned} \tag{4.8b}$$

The final transformation to the normal form

$$\frac{d\xi}{d\tau} = \eta, \tag{4.9a}$$

$$\frac{d\eta}{d\tau} = A\xi^2 + B\xi\eta + C\xi^3 + D\xi^2\eta + E\xi^4 + F\xi^3\eta + O(\|(\xi,\eta)\|^5) \tag{4.9b}$$

is achieved by a time reparameterization combined with a smooth change of coordinates. In this way it is possible to remove both fourth-order terms from (4.9) (using $BC \neq 0$ as will be verified numerically in our case).

The time reparameterization introduces a new time τ as follows:

$$dt = (1 + \theta_1 y_1 + \theta_2 y_1^2)d\tau, \tag{4.10}$$

where θ_1 and θ_2 are to be defined later. Alternatively one can use $(1+\theta_1 y_1+\theta_2 y_2)$ which leads to the same results. The smooth transformation reads

$$\begin{aligned}\xi = {} & y_1 + \frac{1}{2}g_{20}y_1^2 + g_{11}y_1y_2 + \frac{1}{6}g_{30}y_1^3 + \frac{1}{2}g_{21}y_1^2y_2 + \frac{1}{2}g_{12}y_1y_2^2 \\ & + \frac{1}{24}g_{40}y_1^4 + \frac{1}{6}g_{31}y_1^3y_2 + \frac{1}{4}g_{22}y_1^2y_2^2 + \frac{1}{6}g_{13}y_1y_2^3, \end{aligned} \tag{4.11a}$$

$$\begin{aligned}\eta = {} & y_2 + \frac{1}{2}h_{20}y_1^2 + h_{11}y_1y_2 + \frac{1}{6}h_{30}y_1^3 + \frac{1}{2}h_{21}y_1^2y_2 + \frac{1}{2}h_{12}y_1y_2^2 \\ & + \frac{1}{24}h_{40}y_1^4 + \frac{1}{6}h_{31}y_1^3y_2 + \frac{1}{4}h_{22}y_1^2y_2^2 + \frac{1}{6}h_{13}y_1y_2^3, \end{aligned} \tag{4.11b}$$

where g_{ij} and h_{ij} are unknown coefficients. Differentiating (4.11a) and (4.11b) with respect to τ yields

$$\frac{d\xi}{d\tau} = (1+\theta_1 y_1+\theta_2 y_1^2)\left(\frac{\partial \xi}{\partial y_1}\frac{dy_1}{dt} + \frac{\partial \xi}{\partial y_2}\frac{dy_2}{dt}\right), \tag{4.12a}$$

$$\frac{d\eta}{d\tau} = (1+\theta_1 y_1+\theta_2 y_1^2)\left(\frac{\partial \eta}{\partial y_1}\frac{dy_1}{dt} + \frac{\partial \eta}{\partial y_2}\frac{dy_2}{dt}\right). \tag{4.12b}$$

Substituting (4.8a) and (4.8b) into (4.12a) and (4.12b), and then equating coefficients (4.9a) and (4.9b), gives the equations to find the coefficients $g_{ij}, h_{ij}, \theta_1, \theta_2$ in (4.11) and (4.10), as well as A, B, C, D in (4.9), where θ_1 and θ_2 are used to enforce $E = F = 0$. This gives

$$A = \frac{1}{2}b_{20}, \tag{4.13a}$$

$$B = a_{20} + b_{11}, \tag{4.13b}$$

$$C = \frac{1}{6}b_{30} - \frac{1}{2}a_{20}b_{11}, \tag{4.13c}$$

$$\begin{aligned} D = {} & \frac{1}{2}\,b_{21} + \frac{1}{4}\,b_{02}(b_{11}-a_{20}) + \frac{1}{2}\,b_{11}a_{11} + \frac{1}{2}\,a_{30} + \frac{3(a_{20}+b_{11})}{20(3\,a_{20}b_{11}-b_{30})} \\ & \times \big(b_{40} - 6\,a_{20}b_{21} - 3\,b_{11}b_{02}a_{20} + 3\,b_{02}{a_{20}}^2 \\ & \qquad -4\,b_{11}a_{30} + 6\,b_{30}a_{11} + b_{30}b_{02} - 6\,b_{11}a_{20}a_{11}\big)\,. \end{aligned} \tag{4.13d}$$

Note that the third-order coefficient D in (4.9) depends (via b_{40}) on the fourth-order terms of (4.8).

The Taylor coefficient A in (4.9) equals zero, since $b_{20} = 0$ because the critical equilibrium is triple. This implies that one of the nondegeneracy conditions for a classical codimension-two BT point is violated [22, p. 272]. This leads to a bifurcation point with codimension three (or higher) and could, together with the requirement $\det \mathbf{J} = 0$ and $\operatorname{tr} \mathbf{J} = 0$, be used as defining functions to determine the critical parameter values corresponding to this bifurcation point.

If $CD \neq 0$, then the truncated critical normal form

$$\frac{d\xi}{dt} = \eta, \tag{4.14a}$$

$$\frac{d\eta}{dt} = B\xi\eta + C\xi^3 + D\xi^2\eta \tag{4.14b}$$

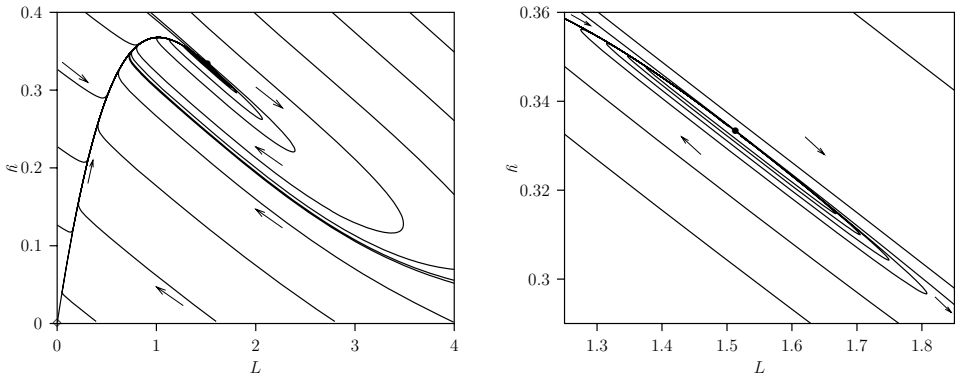

FIG. 4.1. *Phase portrait of* (2.1) *at the critical parameter values with* $b = 2.2$ *(left) and an enlargement of a neighborhood of the critical equilibrium (right), where the elliptic sector is clearly visible.*

can be simplified further by a linear coordinate and time scaling:

$$\frac{d\xi}{dt} = \eta, \tag{4.15a}$$

$$\frac{d\eta}{dt} = \beta\xi\eta + \epsilon_1\xi^3 + \epsilon_2\xi^2\eta, \tag{4.15b}$$

where $\epsilon_1 = \pm 1, \epsilon_2 = \pm 1$, and

$$\beta = \frac{B}{\sqrt{|C|}}.$$

In [2, 12], three topologically different cases are distinguished:

- Saddle case $\epsilon_1 = 1$, any ϵ_2 and β;
- Focus case $\epsilon_1 = -1$ and $0 < \beta < 2\sqrt{2}$;
- Elliptic case $\epsilon_1 = -1$ and $2\sqrt{2} < \beta$.

When $b = 2.2$, the calculated values of the coefficients of the truncated critical normal form (4.14) are $B = 1.0538275511$, $C = -0.110108078$, and $D = -1.23163654$. This gives $\epsilon_1 = -1$ (because $C < 0$), $\epsilon_2 = -1$ (because $D < 0$), and

$$\beta = \frac{B}{\sqrt{-C}} = 3.175849820.$$

We conclude that with $b = 2.2$ the *elliptic case* applies, for $\beta = 3.175849820 > 2\sqrt{2}$. Direct numerical integration of (2.1) at the critical parameter values (3.7) confirms this conclusion (see Figure 4.1).

Calculations showed that in an extended range of parameter values $b > 0$ the parameters C and D defined in (4.14b) are negative, implying $\epsilon_1 = -1$ and $\epsilon_2 = -1$. In Figure 4.2 we give the dependence of β on the parameter b. At $b^\natural = 1.7300228$, where $\beta = 2\sqrt{2}$, there is a transition from the elliptic case to the *focus* case. The phase portrait at the critical parameter values with $b = 1.5$ (when the focus case applies) is depicted in Figure 4.3. Compared with Figure 4.1, where $b = 2.2$, we see that the elliptic sector disappeared.

The transition at $b = b^\natural$ is a bifurcation of codimension four (or higher), which could be considered as the ultimate organizing center in model (2.6). However, in the following we will deal with $b > b^\natural$ corresponding to the elliptic case because it is

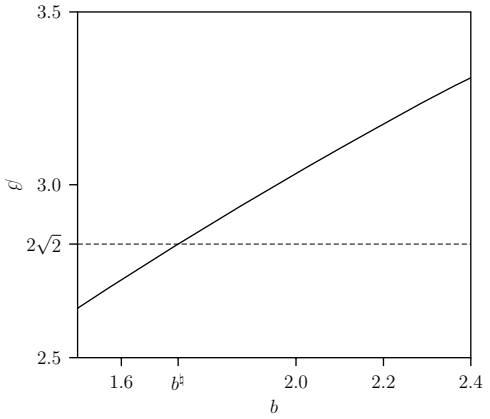

FIG. 4.2. *The coefficient β defined in* (4.15b) *as a function of the parameter b. There is a transition from the elliptic case to the focus case at the codimension-four bifurcation point, where $b = b^\natural = 1.7300228$.*

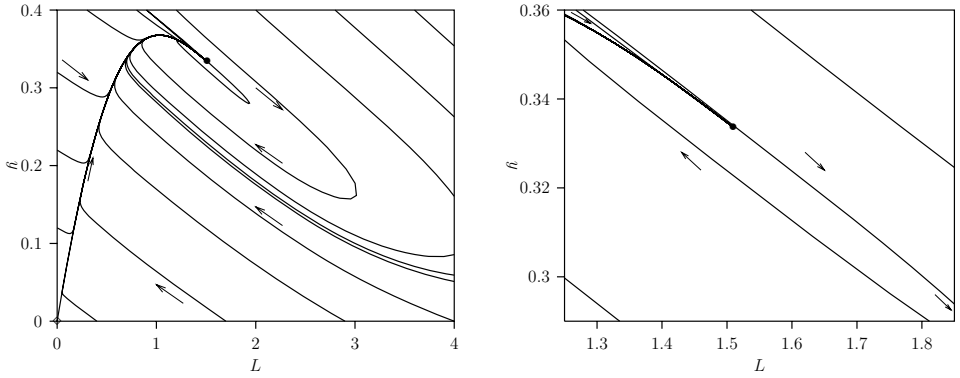

FIG. 4.3. *Phase portrait of* (2.1) *at the critical parameter values with $b = 1.5$ (left) and an enlargement of a neighborhood of the critical equilibrium (right), where no elliptic sector is present.*

the most interesting one. The focus case is discussed extensively in applied literature (for example, in [1, 22] with the analysis of the Rosenzweig–MacArthur predator-prey model having density-dependent mortality rate for the predators, as well as in [13], where an enzyme-catalyzed reaction model is studied). The elliptic case is much less understood, although it has been found in a mathematical model of a reaction of catalytic oxidation in [37].

4.2. Bifurcation diagram of the canonical unfolding. The local bifurcation diagram for the focus and elliptic case has been studied theoretically in [12], where the truncated critical normal form (4.15) is embedded in the following three-parameter family

$$\frac{d\xi}{dt} = \eta, \tag{4.16a}$$

$$\frac{d\eta}{dt} = -\mu_1 - \mu_2\xi + \nu\eta + \beta\xi\eta - \xi^3 - \xi^2\eta, \tag{4.16b}$$

with μ_1, μ_2, and ν serving as the unfolding parameters. Below we reconstruct the

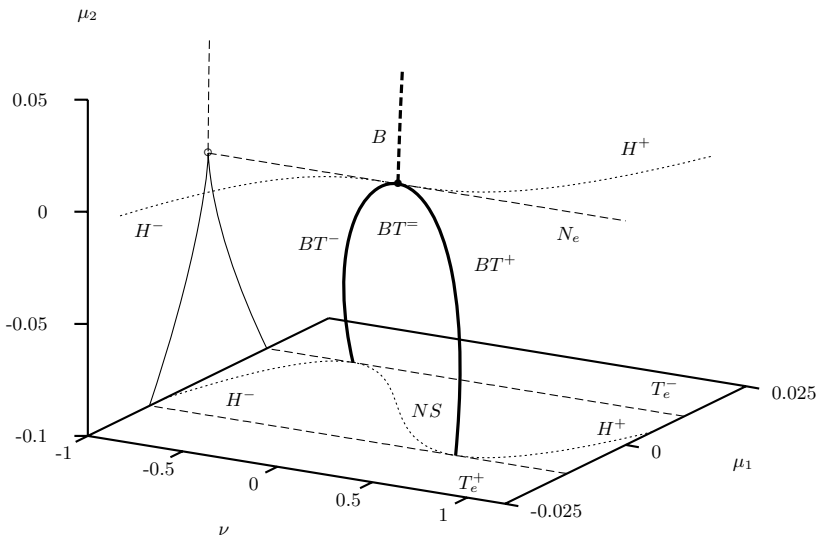

FIG. 4.4. *Three-parameter bifurcation diagram with μ_1, μ_2, and ν as bifurcation parameters for the normal form* (4.16)*, where $\beta = 3.175849820$. Only equilibrium bifurcations are shown. The tangent bifurcation curves $T_e^{\pm}$ (dashed curves) and Hopf $H^{\pm}$ and neutral saddle NS curve (dotted curve) in the (μ_1, ν)-plane for $\mu_2 = -0.1$ are plotted.*

bifurcation diagram of (4.16) in the elliptic case using the same numerical continuation methods as applied in the next section to compute global bifurcation diagrams of (2.1).

The equilibria of (4.16) satisfy $\eta = 0$ and $-\mu_1 - \mu_2\xi - \xi^3 = 0$. Therefore, depending on the parameter values μ_1 and μ_2, there is one or there are three real solutions. For example, when $\mu_1 = 0$, we have $\xi = 0$ and $\xi = \pm\sqrt{-\mu_2}$ besides $\eta = 0$.

In Figure 4.4, a partial three-parameter bifurcation diagram near the codimension-three bifurcation point $\mu_1 = \mu_2 = \nu = 0$ is shown for the normal form (4.16), where $\beta = 3.175849820$ (elliptic case). Two BT curves of different type emanate from the codimension-three point denoted by $BT^=$. Locally attracting limit cycles bifurcate from the first curve which is called a *supercritical Bogdanov–Takens bifurcation curve* and is denoted by BT^-, while repelling limit cycles bifurcate from the curve of second type which is a *subcritical Bogdanov–Takens bifurcation curve*, denoted by BT^+. Another codimension-two bifurcation curve, namely, a cusp curve denoted by N_e in the figure, passes through the point $BT^=$. Finally, from $BT^=$, a codimension-two Bautin (generalized or degenerated Hopf, see [22]) bifurcation curve B emanates. Software packages LOCBIF [18, 22] and CONTENT [25, 15] were used for the numerical continuation of these curves related to equilibrium bifurcations.

Figure 4.5 presents two-parameter slices of the complete bifurcation diagram of (4.16) with $\beta = 3.175849820$ for $\mu_2 = -0.1$ and $\mu_2 = -1$. The left diagram with $\mu_2 = -0.1$ gives a clear picture of the unfolding near the codimension-three BT point. The same diagram (together with corresponding phase portraits) is sketched in Figure 4.6, which we advise to consult while reading the rest of this section. The codimension-two $BT^{\pm}$ points and four saddle-node homoclinic bifurcation points $D_i, i = 1, \ldots, 4$ (analyzed theoretically in [26]) are indicated in all diagrams. These points lie all on the tangent bifurcation curves for equilibria $T_e^{\pm}$. At the supercritical BT^- point, a supercritical Hopf bifurcation curve H^- originates, and similarly a subcritical Hopf bifurcation curve H^+ emanates from the subcritical BT^+. From each BT point, BT^-

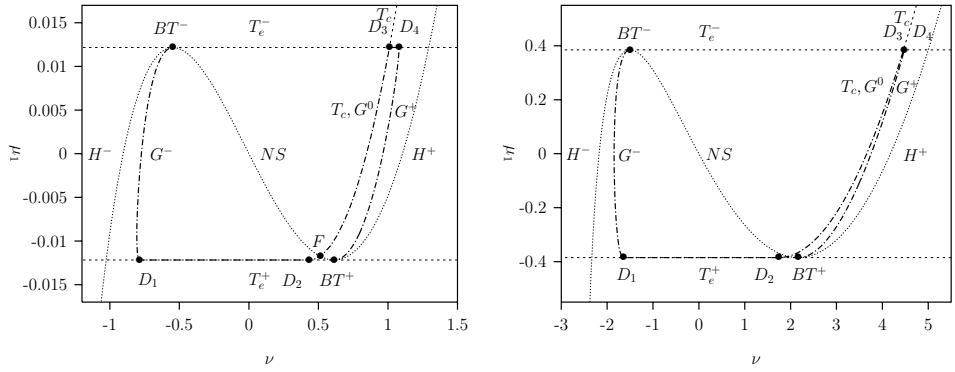

FIG. 4.5. *Two-parameter bifurcation diagrams of* (4.16) *with* μ_1 *and* ν *as bifurcation parameters and* $\mu_2 = -0.1$ *(left) and* $\mu_2 = -1$ *(right) for normal form* (4.16)*, where* $\beta = 3.175849820$*. The labels are explained in the text.*

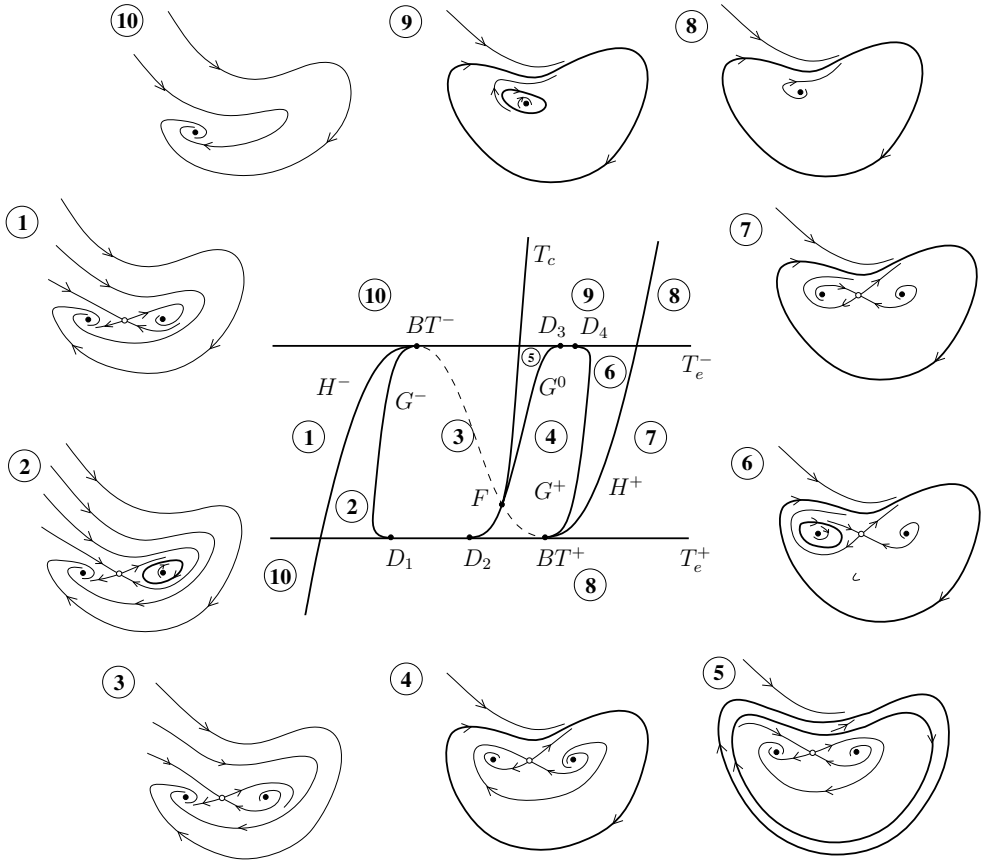

FIG. 4.6. *Schematic bifurcation diagram of* (4.16) *for small* $\mu_2 < 0$ *and* $\beta > 2\sqrt{2}$.

and BT^+, a global bifurcation curve emanates, indicated by G^+ or G^-, respectively. These are saddle homoclinic bifurcation curves. The homoclinic orbits corresponding to them are "small", i.e., they go around one equilibrium only. There exists another

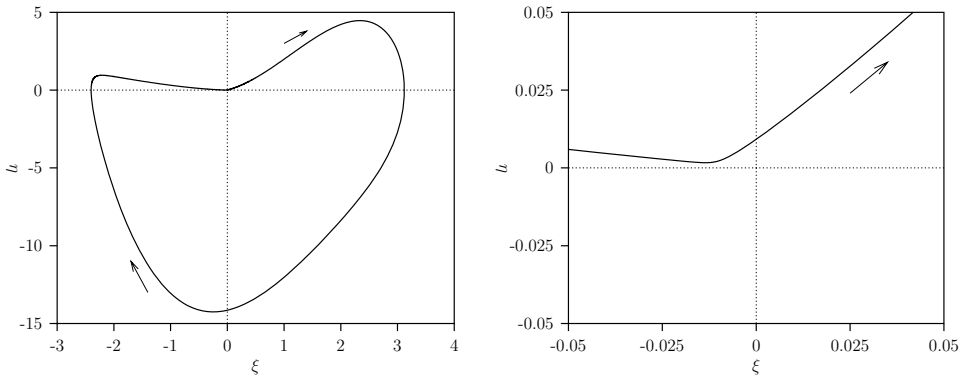

FIG. 4.7. *A nonhyperbolic limit cycle of* (4.16) *at the critical parameter value* $\nu = 0.8458472970$ *corresponding to* T_c *(left) and an enlargement of a neighborhood of the origin, where a saddle equilibrium is located (right). Other parameters are* $\mu_1 = 0, \mu_2 = -0.1, b = 3.175849820$. *We recall that the three equilibria are:* $\eta = 0$ *and* $\xi = 0$ *or* $\xi = \pm\sqrt{0.1}$. *The equilibrium in the origin is a saddle, the left one is stable and the right one unstable.*

saddle homoclinic bifurcation curve, denoted by G^0 in the figure. In contrast with G^+ and G^-, the homoclinic orbit corresponding to G^0 is "big", i.e., it surrounds two equilibria. The homoclinic curves were calculated using the package HOMCONT, a part of AUTO [11]. The implemented theory and numerical procedures are described in [4, 5].

A tangent bifurcation curve for limit cycles T_c, where two limit cycles collide and disappear, crosses the curve T_e^- and ends at a point F in the intersection of the homoclinic curve G^0 and the neutral saddle curve NS connecting the Bogdanov–Takens points BT^- and BT^+. This point F corresponds to a codimension-two "big" homoclinic orbit to a neutral saddle, where the trace of the Jacobian matrix is zero [22]. The tangent bifurcation curve for limit cycles T_c and the homoclinic curve G^0 have an infinite-order contact at F [29]. It should be noted that T_c is indistinguishable from G^0 in Figure 4.5. Between the equilibrium bifurcation curves T_e^+ and T_e^-, the curve T_c is located just above G^0. This can be verified by accurate computations in AUTO or CONTENT with many mesh points (e.g., `NTST=1000`). Figure 4.7 demonstrates that the critical limit cycle corresponding to T_c is located at a small but clearly visible distance from the saddle equilibrium at the origin. This nonhyperbolic limit cycle bifurcates into (outer) stable and (inner) unstable limit cycles, shown in Figure 4.8 for parameter values between the curves T_c and G^0. When we cross the homoclinic bifurcation curve G_0 above point F, the inner unstable limit cycle "collides" with the saddle and disappears via the saddle homoclinic orbit that is unstable from the outside, in accordance with the positive sign of the trace of the Jacobian matrix above the curve NS (see Figure 4.5). Crossing G^0 below F results in the appearance of a stable "big" cycle.

The saddle homoclinic curve G^-, originating at the point BT^-, terminates tangentially at a point D_1 on the bifurcation curve T_e^+. Between the two codimension-two points D_1 and D_2 the saddle-node equilibrium (existing along the tangent bifurcation curve T_e^+) has a smooth homoclinic orbit. On this line segment D_1D_2, the global bifurcation and the local bifurcation occur simultaneously. The homoclinic orbit is asymptotic to a saddle-node rather than to a saddle. In point D_2, the "big" saddle homoclinic curve G^0 departs tangentially from T_e^+. This curve G^0 ends also tangen-

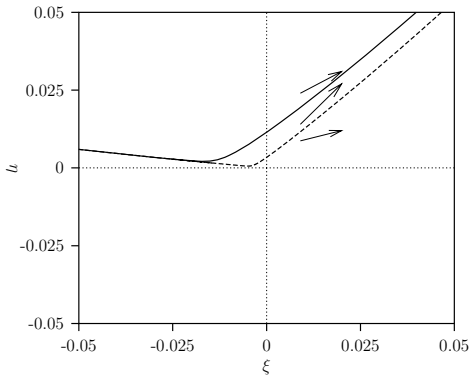

FIG. 4.8. *A stable limit cycle (outer, solid) and an unstable (inner, dashed) limit cycle of* (4.16) *at* $\nu = 0.8458473000$. *The other parameters are* $\mu_1 = 0, \mu_2 = -0.1, b = 3.175849820$.

tially at a codimension-two point D_3 on T_e^-, which is similar to D_2. Another saddle homoclinic curve, G^-, originating at BT^+ on the bifurcation curve T_e^+, terminates tangentially at a point D_4 on T_e^-. In all points D_i, the corresponding homoclinic orbits are nonsmooth at the saddle-node. The right diagram with $\mu_2 = -1$ shows that already in the vicinity of the codimension-three point the two saddle-node homoclinic bifurcation points D_3 and D_4 are also close to each other and hardly distinguishable in Figure 4.5.

4.3. Elliptic versus focus case. The bifurcation diagram of the normal form (4.16) presented in Figure 4.6 differs drastically from the theoretical bifurcation diagram for the elliptic case given in [12, p. 8]. The reason for this discrepancy is that the diagram in [12] concerns phase portraits in a *fixed* small neighborhood (in fact, an elliptic disk) of the origin. Therefore, additional bifurcation curves associated with boundary tangencies appear, while some parts of the global bifurcation curves described above become "invisible," since the corresponding bifurcations happen outside the neighborhood. This approach is absolutely legitimate in theoretical studies, but is of little use in applied analysis, where artificial boundaries have no meaning and global phase portraits in the whole phase plane must be considered. Only such portraits could provide a good understanding of the long-term dynamics of the model.

Figure 4.5 gives such global bifurcation diagrams of the normal form (4.16). It turns out that the two-parameter slices are topologically equivalent to those corresponding to the focus case (see [2, p. 36] or [12, p. 7], where an intersection of bifurcation surfaces with a small sphere centered at the origin in the three-dimensional parameter space is shown). However, the inner limit cycle demonstrates rapid amplitude changes ("canard-like" behavior) near the bifurcation curve T_c. It is this phenomenon that makes the continuation of limit cycles near T_c difficult. One could also observe that, in contrast with the focus case, the "big" homoclinic orbit to the neutral saddle (see point F) does not shrink to the origin of the phase plane, when we approach the codimension-three elliptic BT point in the parameter space. Instead, this homoclinic orbit tends to the boundary of the elliptic sector that has a finite size in (4.16). The similarity between the focus and the elliptic cases implies that the transition between them at $b = b^\natural$, although interesting from a theoretical point of view, is of minor importance in applications, since it does not affect dynamics away from the degenerate BT bifurcation points.

These similarities and differences between the focus and the elliptic cases were overlooked in all theoretical studies. Of course, global phase portraits arising from an elliptic BT case in a specific model could differ from the global bifurcation diagrams of the canonical unfolding (4.16) reported above. However, if other phase objects (equilibria, cycles, etc.) do not interact with the objects bifurcating around the codimension-three BT point, one would encounter the described bifurcation diagrams in his/her system, as it happens in our ecological model (2.1).

5. Bifurcation diagrams of (2.1). To facilitate our understanding of the bifurcation structure, we construct three-, two-, and one-parameter bifurcation diagrams of (2.1) for a representative parameter value $b = 2.2$ (elliptic case). We also show explicitly various homoclinic orbits.

5.1. Three-parameter bifurcation diagram. In Figure 5.1, the three parameters μ, m, a are changed simultaneously. There is a codimension-three point, denoted by $BT^{=}$ at the critical parameter values $(\mu^\sharp, m^\sharp, a^\sharp)$ given by (3.7). The bifurcation pattern resembles that of the normal form (4.16) presented in Figure 4.4. There is now another codimension-two Bautin bifurcation curve B which is not connected to a codimension-three point $BT^{=}$. Varying the fourth parameter b showed that such a connection never occurs in the region of the parameter space of interest in this paper.

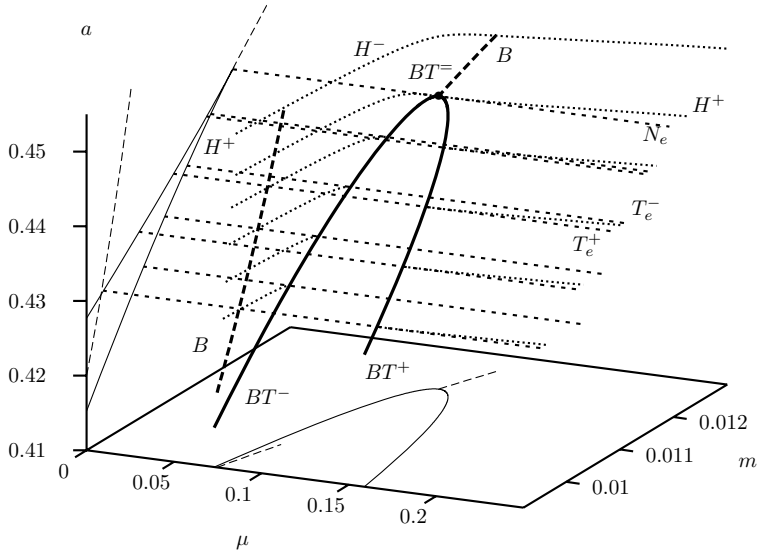

FIG. 5.1. *Three-parameter bifurcation diagram for equilibria of* (2.1) *with* μ, m *and* a *as bifurcation parameters. The codimension-three Bogdanov–Takens point is denoted by* $BT^{=}$. *From this point two codimension-two BT curves,* BT^{-} *and* BT^{+}, *emanate. They are shown along with their projections. The codimension-two Bautin bifurcation curves* B *are long dashed. The Hopf bifurcation curves (dotted) and tangent bifurcation curves (short dashed) are shown for* $a = 0.455$, $a = 0.4492277$, $a = 0.44$ *and* $a = 0.43$. *The curve* N_e *passing through* $BT^{=}$ *is a cusp bifurcation curve for equilibria. The two curves* $T_e^{\pm}$ *for* $a = 0.44$ *are the intersections of the* $a = 0.44$ *plane with the tangent bifurcation surfaces. Similarly the* H^{+} *and* H^{-} *curves from the intersections for the two-dimensional Hopf bifurcation surfaces. For a-values above the point* $BT^{=}$ *these sheets are separated by the codimension-two Bautin bifurcation curves* B. *These sheets are separated for a-values below the point* $BT^{=}$, *where the two codimension-two BT curves,* BT^{-} *and* BT^{+}, *form the end curves of the separated sheets. For smaller* μ*-values there is always a codimension-two Bautin bifurcation curve* B *that separates super- and subcritical Hopf bifurcation surfaces.*

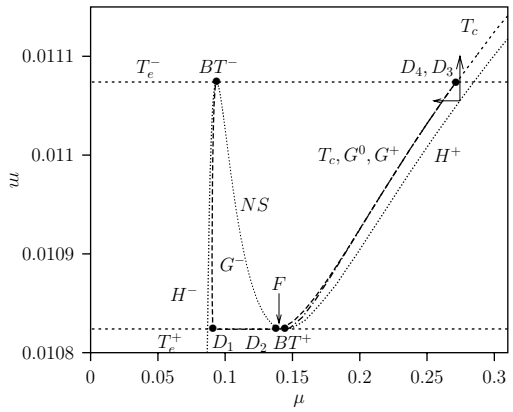

FIG. 5.2. *Two-dimensional bifurcation diagram with μ and m as bifurcation parameters, where $a = 0.44$.*

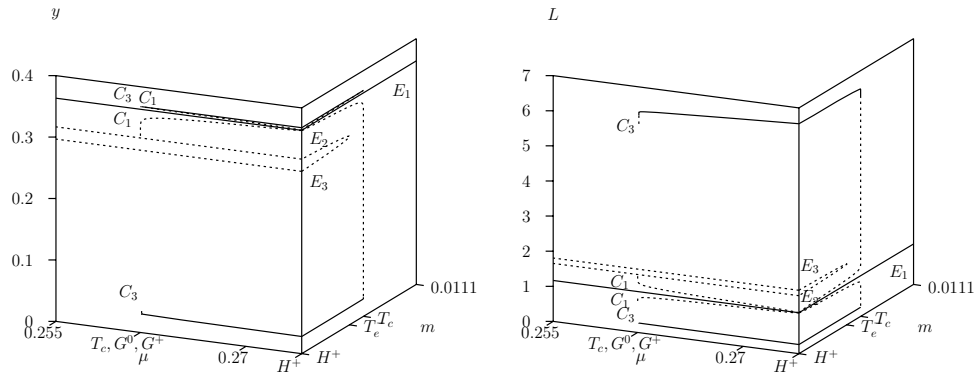

FIG. 5.3. *Combined bifurcation diagrams for region around bifurcation point D_3, where $a = 0.44$. The bottom right vertex, for both y and L, corresponds to the point $\mu = 0.2743923$ and $m = 0.01105501$ on the Hopf bifurcation H^+ in Figure 5.2.*

Codimension-one bifurcation curves for $a = 0.44$ and for the reference value $a = 0.43$ are investigated in the next section using two-parameter bifurcation diagrams.

5.2. Two-parameter bifurcation diagram. The two-parameter bifurcation diagram for $a = 0.44$ in Figure 5.2 strongly resembles that given in Figure 4.5 (right), where $\mu_2 = -1$. The Hopf bifurcation curves H^- (origination to the left in BT^-) and H^+ (origination to the right in BT^+), the neutral-saddle curve NS (between BT^- and BT^+), and the tangent bifurcation curves $T_e^{\pm}$ (straight lines parallel to the ν-axis) as well as the tangent bifurcation curve for limit cycles T_c are shown. Observe that although the parameter value $a = 0.44$ is rather close to $a^\sharp$, the two saddle-node homoclinic bifurcation points D_3 and D_4 are indistinguishable in the figure. In two one-parameter bifurcation diagrams with respect to μ and m combined in Figure 5.3, the extrema of the cycles in the region close to points D_3 and D_4 are plotted. The two homoclinic bifurcations for the cycles C_1 and C_3 are connected via the tangent bifurcation of these cycles at T_c. This explains how the large amplitude cycle C_3 surrounding all three equilibria, E_1, E_2, and E_3, appears. The tangent bifurcation

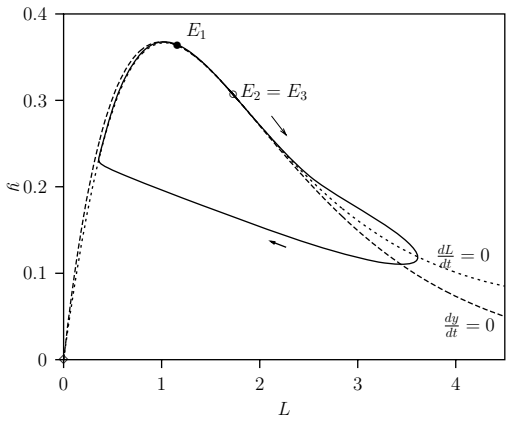

FIG. 5.4. *Phase-plane plot for parameter values between the codimension-two points D_3 and D_4, $\mu = 0.2714740$ and $m = 0.01107377$ for $a = 0.44$. Also the two isoclines are shown. These intersect in the two equilibria, namely, the saddle-node, where two points E_2 and E_3 coincide, and the unstable equilibrium E_1.*

curve T_c for limit cycles goes all the way down to the point F corresponding to the homoclinic orbit to a neutral saddle. Between the lines $T_e^{\pm}$, T_c is very close to the "big" homoclinic curve G^0.

A smooth homoclinic orbit to a saddle-node on the tangent bifurcation curve T_e^- between the points D_3 and D_4 is depicted in Figure 5.4. Also the isoclines are drawn. The homoclinic orbits locally coincide with a center manifold W^c of the saddle-node $E_2 = E_3$ and is therefore smooth. The orbit approaches and leaves the saddle-node via the center manifold, that is, it is tangent to the eigenvector belonging to the zero eigenvalue of the saddle-node on T_e^-. At the points D_3 and D_4 the homoclinic bifurcation curves G^+ and G^0 terminate at the equilibrium tangent bifurcation curve T_e^-, where the equilibria E_3 and E_2 coincide. At these points, the homoclinic orbit to the saddle-node is nonsmooth.

Figure 5.5 shows a two-parameter bifurcation diagram where μ and m are again the bifurcation parameters, while now $a = 0.43$. The two-parameter bifurcation diagram in Figure 5.5 resembles that for $a = 0.44$ given in Figure 5.2 except that there are no points D_3, D_4. If the values of the parameter a are lower, the Hopf bifurcation H^+ does not intersect the curve T_e^-. One can show that H^+ has a horizontal asymptote as $\mu \to \infty$, namely, the line $m = m_\sharp = 0.01026241193$. Furthermore, the curve G^- originating at BT^- and terminating at D_1 follows closely the Hopf bifurcation curve H^-. Figure 5.6 is an expanded view of Figure 5.5 in the region of the the two points D_1 and D_2. The tangent bifurcation curve T_c for limit cycles is indistinguishable from the segment of G^0 located above the point F also in Figure 5.6.

5.3. One-parameter bifurcation diagrams. In Figures 5.7 and 5.8, where $m = 0.01, a = 0.43$, the bifurcation parameter is μ. For all μ-values, there are three interior equilibria, denoted by E_1, E_2 and E_3, the positions of which are independent of μ. For the (scaled) numbers of juveniles and adults at these equilibria, $E_j = (L_j^*, y_j^*)$, we have $L_1^* < L_2^* < L_3^*$ and $y_1^* > y_2^* > y_3^*$, respectively. Hopf bifurcations of E_1 and E_3 occur at H^+ and H^-, respectively, giving rise to limit cycles. Their maximum and minimum values are plotted in the figure, a stable one, denoted by C_3 and generated by the supercritical Hopf bifurcation from the equilibrium E_3 and an unstable one,

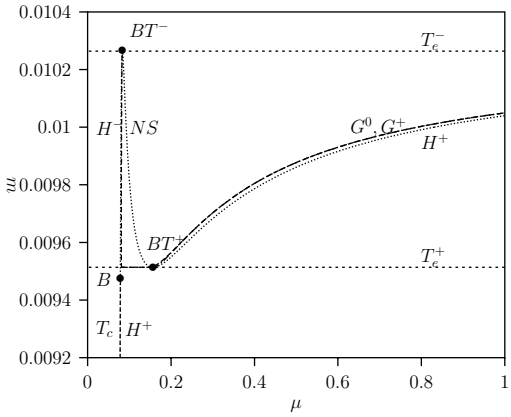

FIG. 5.5. *Two-parameter bifurcation diagram with μ and m as bifurcation parameters, where $a = 0.43$. At the Bogdanov–Takens codimension-two point BT^-, a tangent (T_e^-), supercritical Hopf (H^-) and a homoclinic curve (G^-) meet. Similarly, at the point BT^+, a tangent (T_e^+), subcritical Hopf (H^+) and a homoclinic curve (G^+) meet. At the Bautin codimension-two point B, a tangent bifurcation for the limit cycle T_c originates. For more details, see Figure* 5.6.

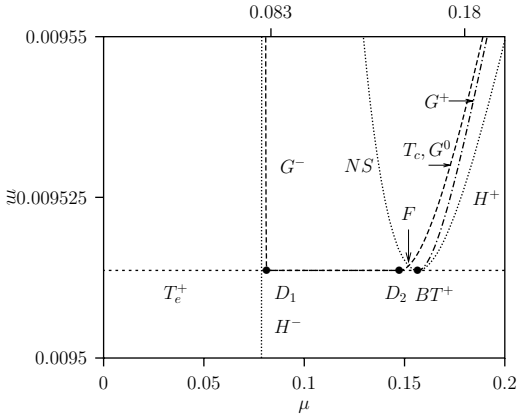

FIG. 5.6. *The Hopf bifurcation curve H^- (dotted) and the tangent bifurcation T_e^+ (short dashed) are shown. Further, the homoclinic bifurcation curve G^- which originates from BT^- (shown in Figure* 5.5*), and the homoclinic bifurcation curve G^+ (dashed-dotted) which originates from BT^+ ($\mu = 0.1566$) together with T_e^+ are shown. Between the codimension-two points D_1 ($\mu = 0.1474$) and D_2 ($\mu = 0.0813$), there is a smooth saddle-node homoclinic orbit. The tangent bifurcation curve T_c for limit cycles is indistinguishable from the segment of the homoclinic curve G^0 located above the point F.*

denoted by C_1 and generated by the subcritical Hopf bifurcation from the equilibrium E_1. For large μ, there is a branch of "big" stable periodic orbits (also denoted by C_3) which surround all three equilibria. This branch also exists for μ values for which the unstable period orbits C_1 surrounding the equilibrium E_1 exist. There are homoclinic orbits at the points where these limit cycles touch the saddle equilibrium E_2.

In Figure 5.9, we show the one-parameter diagram for fixed $\mu = 0.08337$ with m as the bifurcation parameter. The parameter μ has been chosen in such a way that it lies between the μ-coordinates of the codimension-two points D_1 and D_2 in Figure 5.6, where a saddle-node homoclinic bifurcation occurs. In this global bifurcation curve,

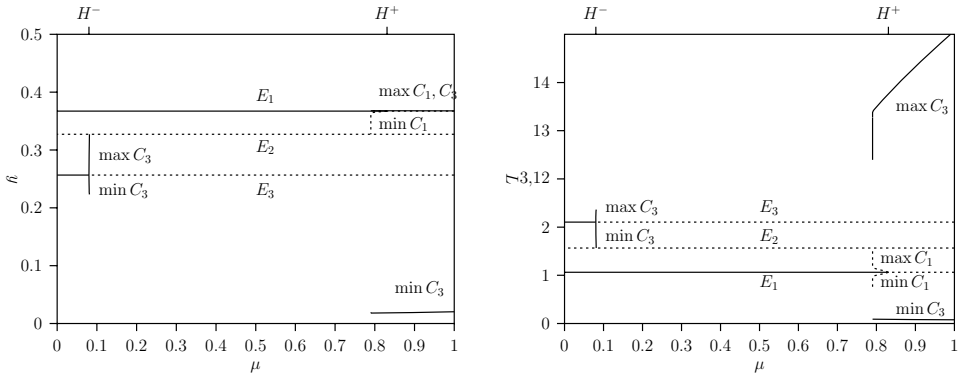

FIG. 5.7. *Bifurcation diagram, where $m = 0.01$ and $a = 0.43$, and μ is the single bifurcation parameter. Stable equilibria are represented by solid lines and unstable equilibria by dashed lines which are horizontal because the y and L equilibrium values are independent of μ. A branch of stable limit cycles C_3 (solid curves) originate through the supercritical Hopf (H^-), and a branch of unstable limit cycles C_1 (dashed curves) through the subcritical Hopf bifurcation (H^+). A homoclinic orbit occurs where these limit cycles touch the saddle equilibrium E_2.*

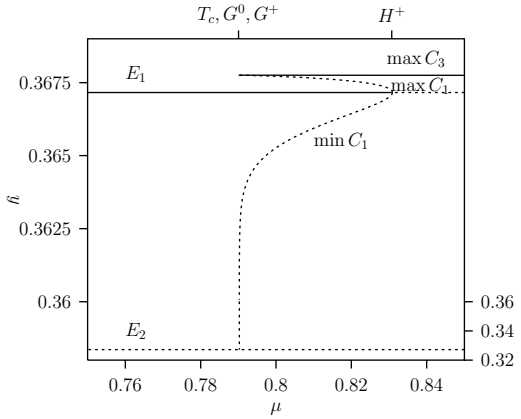

FIG. 5.8. *Detail of Figure 5.7. The solid curve is the maximum of the large amplitude cycle C_3. The dashed curve is the unstable limit cycle C_1 that emanates from the Hopf bifurcation point H^+. In order to get a better plot, the scaling of the y-axis below $y = 0.36$ is changed. The two homoclinic bifurcations G^0 and G^+, as well as the tangent bifurcation T_c of limit cycles, occur at almost the same value of μ.*

also a local tangent bifurcation T_e^+, where the two equilibria E_1 and E_2 coincide, is involved. The time-averages of the limit cycles are plotted. The stable limit cycle C_3 disappears when the average reaches the tangent point at T_e^+. This is explained in Figure 5.10, where the homoclinic orbit in the phase plane is shown for parameter values of m at the saddle-node homoclinic bifurcation. The homoclinic orbit is similar to that shown in Figure 5.4 for a point between the two codimension-two points D_3 and D_4.

A periodic solution $(L(t), y(t))$ near the saddle-node homoclinic orbit stays close to a point where the saddle-node will appear for most of its period, then completes the orbit by making a rapid and large excursion in the phase plane. Hence the time-average for one period is approximately the equilibrium value. This explains why it

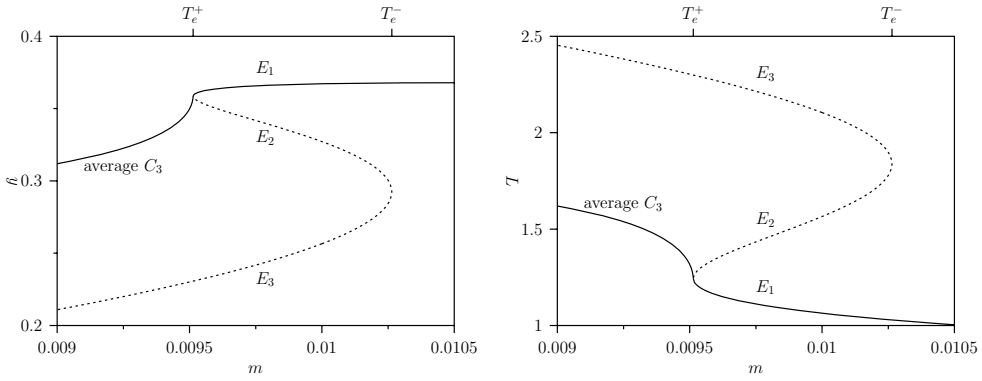

FIG. 5.9. *Bifurcation diagrams for* $y = \frac{\mu}{m}A$ *and* L *with* m *as bifurcation parameter for* $\mu = 0.08336837$ *and* $a = 0.43$. *Stable equilibria (solid curve) and unstable equilibria (dashed curve) as well as the time-averages for the stable limit cycle (solid curve) are plotted. Stable limit cycles originate in the supercritical Hopf* (H^-) *bifurcation shown in Figures* 5.5 *and* 5.6. *These cycles terminate at a smooth saddle-node homoclinic orbit.*

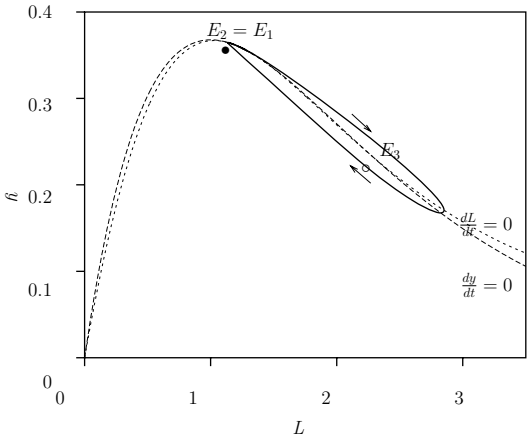

FIG. 5.10. *Phase portrait for* $\mu = 0.083$, $a = 0.43$ *and* $m = 0.009513629$. *The smooth homoclinic orbit to the saddle-node equilibrium* $E_1 = E_2$ *coincides locally with a center manifold of this point. Also, the unstable equilibrium* E_3 *inside the homoclinic orbit and two isoclines are shown.*

is advantageous to plot the time-averages in addition to the maximum and minimum values. Observe that y becomes small during the excursion but this occurs over a relatively (the period T goes to infinity) short time interval. Note that the unstable manifold of the saddle E_2 can go to E_1 directly or via a "big" loop around E_3 similar to the saddle-node homoclinic orbit shown in Figure 5.10.

Figure 5.11 is a one-parameter diagram, where m is the bifurcation parameter for $\mu = 1.0$ and $a = 0.43$. It shows how the three interior equilibria are connected. There are two tangent bifurcations $T_e^{\pm}$, where two equilibria coincide. A subcritical Hopf bifurcation of E_1 occurs at H^+, generating a branch of unstable limit cycles, denoted by C_1, while a supercritical Hopf bifurcation of E_3 occurs at H^-, generating a branch of stable limit cycles, denoted by C_3. The maximum and minimum values for both branches have been plotted in the figure. Varying m, this unstable limit cycle touches the saddle E_2 in a homoclinic orbit.

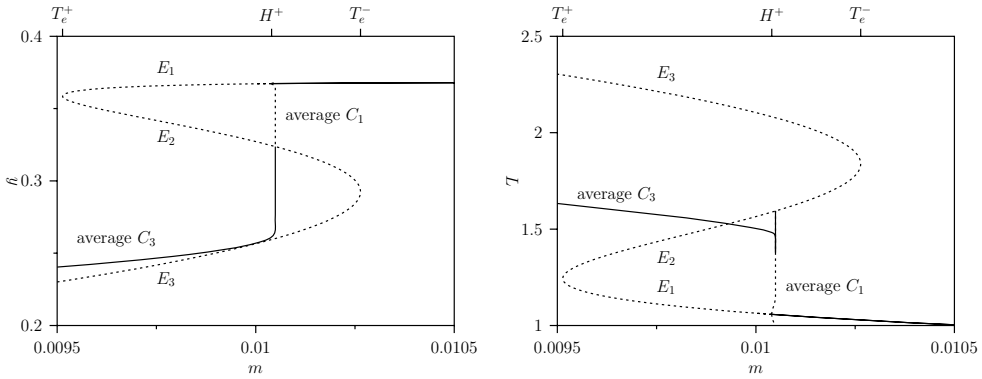

FIG. 5.11. *Bifurcation diagrams for $y = \frac{\mu}{m}A$ and L with m as bifurcation parameter, where $\mu = 1.0$ and $a = 0.43$. Stable equilibria (solid curve) and unstable equilibria (dashed curve) as well as the time-averages for the stable limit cycles (solid curve) and for the unstable limit cycles (dashed curve) are plotted.*

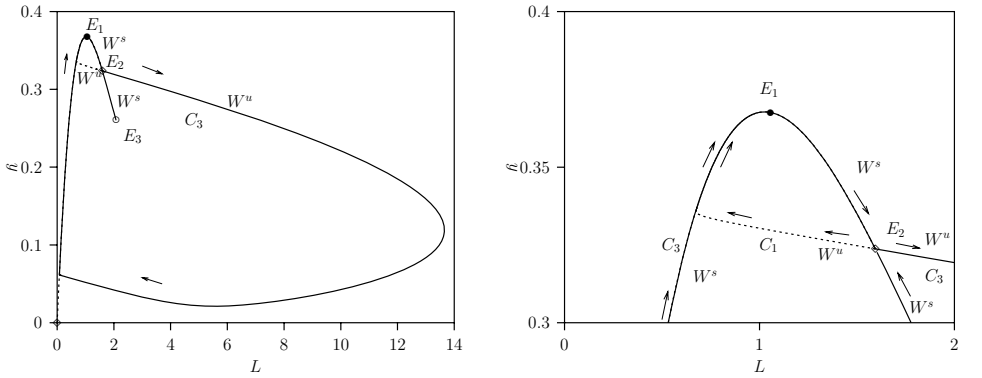

FIG. 5.12. *Two homoclinic orbits and time-evolution for $\mu = 1.0$ and $a = 0.43$, where $m = 0.01004953$ and $m = 0.01004952$ for large amplitude and small amplitude orbits, respectively. The right figure is an expanded view of the left figure. The stable W^s and unstable W^u manifolds of the saddle point indicated by a $\diamond$ are shown. The stable focus E_1 is indicated by a bullet and the source E_3 by a circle. Here the flow direction is indicated by arrows for the stable homoclinic orbit C_3 at the outside and for the unstable homoclinic orbit C_1 at the inside.*

Furthermore, the average values for the limit cycle C_3 are plotted. The unstable cycle C_3 originates in the supercritical Hopf bifurcation H^- of equilibrium E_3. Both average curves touch the saddle curve E_2. The average curve as a function of m for the stable limit cycles C_3 is very steep close to the bifurcation point. The average L-values first decrease before increasing up to the saddle-point value. This is most clear from the graphs $y(m)$ and $L(m)$. Actually, the cycle C_3 becomes unstable via a tangent limit cycle bifurcation not show in the figure. Both homoclinic bifurcations occur in very close proximity.

Figure 5.12 shows approximations of these two homoclinic orbits, one "big" (solid) C_3 and one "small" (dashed) C_1. The period of the plotted limit cycles is very large, indicating a homoclinic orbit. There are two rather sharp bends in the "big" homoclinic orbit. The top one is close to the saddle point as expected. The lower bend is associated with the zero equilibrium $(L = 0, y = 0)$ which is a saddle point for the parameter values used. Both orbits pass the stable focus E_1 closely.

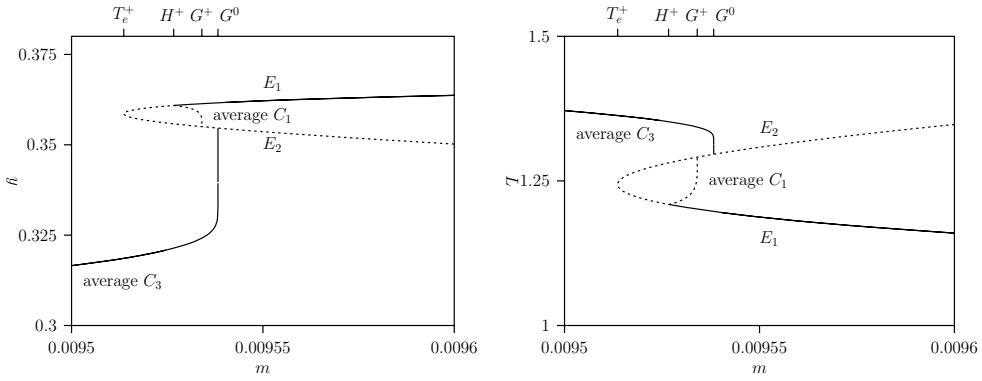

FIG. 5.13. *Bifurcation diagrams for $y = \frac{\mu}{m}A$ and L with m as bifurcation parameter, where $\mu = 0.18$ and $a = 0.43$. Stable equilibria (solid curve) and unstable equilibria (dashed curve) as well as the time-averages for the stable limit cycle (solid curve) and for the unstable limit cycle (dashed curve) are plotted.*

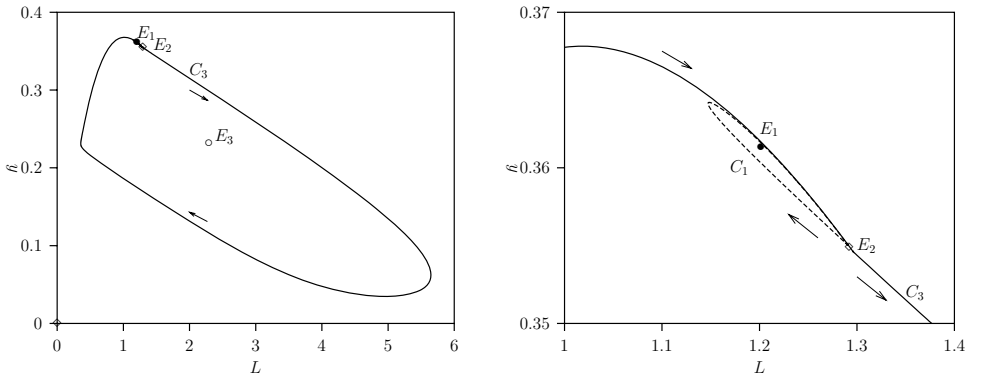

FIG. 5.14. *Phase portrait for $\mu = 0.18$ and $a = 0.43$. Left: Where $m = 0.009534053$, there is a "big" homoclinic orbit C_3. Right: An expanded view of the homoclinic orbit C_3 (solid curve) close to saddle E_2. For $m = 0.009538250$, in the same plot the "small" homoclinic orbit C_1 (dashed curve) is shown.*

In order to get more detailed information on the dynamics close to the homoclinic orbits, we study the one-parameter diagram for fixed $\mu = 0.18$, where m is varied (see also Figure 5.6).

In Figure 5.13, the average values of the variables for the limit cycles are plotted together with their equilibrium values. For m values below the Hopf bifurcation H^+, the large amplitude stable limit cycles, whose averaged values form the curve C_3, are globally attracting. For m values above the curve H^+, the unstable limit cycles C_1 which emanate from E_1 at the Hopf bifurcation H^+ are separating boundaries. Starting outside the limit cycle results in convergence to the stable limit cycle C_3, but starting inside the limit cycle gives convergence to the stable equilibrium E_1. Increasing m, this bistability persists until the unstable limit cycle (averaged C_1) disappears abruptly at the global bifurcation G^+ via the homoclinic orbit shown in Figure 5.14. For parameter values m above G^+, there is still bistability of the stable equilibrium E_1 and the stable limit cycle C_3, but now the stable manifold of the saddle equilibrium E_2 acts as the separatrix.

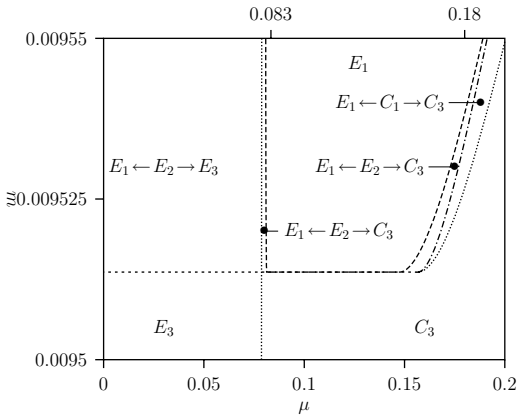

FIG. 5.15. *Attractors in some regions of the two-parameter bifurcation diagram shown in Figure 5.6.* $E_1 \leftarrow E_2 \rightarrow E_3$ *means bistability of the two equilibria* E_1 *and* E_3 *and the stable manifold of the saddle* E_2 *is the separatrix.*

In Figure 5.15 several attractors for typical points in the two-parameter bifurcation diagram Figure 5.6 are indicated. The regimes are all separated by codimension-one curves as shown in Figure 5.6. For small μ values, there is bistability of the two equilibria E_1 and E_3 and the stable manifold of the saddle E_2 is the separatrix. This region is labeled $E_1 \leftarrow E_2 \rightarrow E_3$. For larger μ values there is bistability of the equilibrium E_1 and the limit cycle C_3, while the stable manifold of either the saddle E_2 ($E_1 \leftarrow E_2 \rightarrow C_3$) or the unstable limit cycle C_1 ($E_1 \leftarrow C_1 \rightarrow C_3$) is a separatrix. Note that C_3 can surround either just E_3 or all three equilibria, E_1, E_2, and E_3.

6. Discussion. We have considered the most basic model for stage-structured populations in which per capita transition from the juvenile into the adult class is density dependent, namely, a system of two ordinary differential equations. This model was originally suggested in [21]. Birth pulses have been added in [33], but we are only interested in the time-autonomous case here. Alternative more sophisticated models involve differential-delay equations with density-dependent delays [17], transport equations with density-dependent speed [27, 8], difference equations [3, 6, 7], and integral equations with density-dependent transition kernels [10]. We refer to [20] for a review of the different model formulations and their relationships. While more complex models also exhibit more complex behavior than simple models, the complex behavior may be more difficult to detect and track due to the large number of parameters and initial conditions inherent in such systems.

In [21], periodic orbits were found which surround a unique interior equilibrium. Up to three interior equilibria, two of which can undergo Hopf bifurcation, were discovered in [34, sect. 11]. In order to determine more systematically the dynamics of our planar system (2.6), we have performed a four-parameter bifurcation analysis under the assumption of pure intrastage competition. To report our results, we fix a representative value of parameter b that characterizes the birth rate of adults and then presents the three-parameter bifurcation diagrams. These are the three parameters which we have varied. The parameter a is related to the average number of offspring produced by one typical adult if there is no competition. The parameter μ represents the per capita mortality rate of juveniles. The parameter m has no direct interpretation, but $p_0 = \frac{1}{1+m}$ is the probability of surviving the juvenile stage under

no competition. The parameter a determines the shape of a function M involved in the equation $M(L^*) = m$ which determines the juvenile coordinate L^* of an interior equilibrium. Depending on a, M can be either strictly monotone decreasing in $L^* \geq 0$ or decreasing for small L^*, increasing for intermediate L^*, and decreasing again for large L^*. The $a = a^\sharp$ value at which M undergoes the transition is the a-coordinate of a codimension-three BT bifurcation point which is the organizing center of our three-parameter bifurcation diagrams. There exists a unique $L^* > 0$ such that $M'(L^*) = M''(L^*) = 0$. L^* is the juvenile coordinate of a saddle-node. $m = M(L^*)$ is the m coordinate of the degenerate BT point. Its μ-coordinate is determined by making 0 a double eigenvalue of the Jacobian matrix. This leads to the following procedure for calculating the position of the codimension-three BT bifurcation point. When b is fixed, there are five unknowns, namely, two equilibrium values for the state variables, $L^\sharp, y^\sharp$ and three parameters $a^\sharp, m^\sharp, \mu^\sharp$. There are two equilibrium equations (right-hand sides of (2.6) zero), the requirements that the determinant and trace of the Jacobian matrix evaluated at the equilibrium point are zero and the additional requirement that $M''(L^\sharp) = 0$. The first four are necessary for a codimension-two BT point, while the latter is satisfied at a codimension-three BT point. Surprisingly, the latter condition is a geometrical one (the position of the inflection point of a function $M(L^*)$ defined in (3.1)). The function $M(L^*)$ is the expression for a parameter, m, derived from the equilibrium equation for one state variable, L, where the solution of the other state variable, $y^*(L^*)$, from the second equilibrium equation is substituted. We use the fact that $M(L^*)$ and $y^*(L^*)$ formulations are explicit as is the case with the population model (2.6). Commonly it is the requirement that one coefficient of a higher-order term of a Taylor series expansion equals zero (see [22, p. 272] for details). In this paper we established existence of a codimension-three BT bifurcation in our model and have verified its nondegeneracy by computing its normal form numerically.

The normal form is computed using a preliminary linear transformation to simplify the linear terms, in this case to put the linear part in the Jordan canonical form. In [22, 23] this step is omitted by using a representation of any vector in the state space as a linear combination of the eigenvector and the adjoint eigenvector. That method is appropriate for higher-order dynamics systems where normalization on the center manifold is needed [24]. The nonlinear smooth transformation in this paper is combined with a time reparameterization. This facilitates the removal of all fourth-order terms in the Taylor series expansion. Therefore the expression for the coefficient D of the $\xi^2\eta$ term given by (4.13d) differs from the classical expression [19], where only third-order terms are taken into account. The expressions (4.13) agree with those reported in [14]. In this way, we have computed the relevant normal form coefficients and established that the critical equilibrium at the codimension-three BT point is triple and has an elliptic sector for $b > b^\natural = 1.7300228$. Apparently, this case has never been observed in ecological modeling. At $b = b^\natural$, a transition from the elliptic codimension-three BT to the focus codimension-three BT point occurs.

Using known theoretical results [2, 12], we have concluded that two BT codimension-two curves emanate from the codimension-three BT point. Along these curves a Hopf bifurcation surface, as well as a tangent bifurcation and a homoclinic orbit surface, meet. There is also a codimension-two Bautin bifurcation curve B in the Hopf bifurcation surface, where the supercritical Hopf bifurcation becomes subcritical or vice versa. This happens in a parameter region where only one interior equilibrium exists. In Bautin bifurcation points, a surface of tangent bifurcations of limit cycles originates.

Our numerical analysis of the global bifurcation diagram of the canonical unfolding of the normal form, Figure 4.5, has revealed other global bifurcation curves. On codimension-two bifurcation curves D_i, transitions of the homoclinic orbit to a saddle-node homoclinic orbit occur. There is also a bifurcation surface G^0 corresponding to a "big" homoclinic orbit to the saddle that surrounds two equilibria. In this surface, a line F of codimension-two homoclinic orbits to a neutral saddle exists. Figure 5.2 resembles that of the Bazykin's predator-prey model [1, Fig. 3.5.3] and [22, Fig. 8.10], despite the fact that the degenerate BT point is here of the elliptic type while in Bazykin's model it is of the focus type. The diagrams given in [12] for both types differ a lot on first sight. However, in [12] additional bifurcation curves associated with boundary tangencies are reported. In this paper, we do not have such artificial bifurcations, since we do not restrict our attention to a small neighborhood of the critical equilibrium. Instead, we consider global phase portraits, which allows us to obtain a better understanding of the long-term dynamic behavior of the model. It should be stressed that without a preliminary analysis of the canonical unfolding (4.16) it would have been practically impossible to understand the numerical continuation results for (2.6).

A large-time solution behavior of similar complexity has been found for certain planar predator-prey systems [1, 22, 38, 31, 39] and epidemic models [30]. Predator-prey and host-parasite systems involve two species which influence each other in opposite ways with one suffering while benefiting the other. The predator-prey models which show complex behavior take into account competition among prey and predator competition for prey. Our model involves two stages of one species which compete among themselves but influence each other positively because we assume pure intra-stage competition. (Adding interstage competition actually counteracts the complexity.) Mathematically, this is reflected in the fact that the nonlinear terms in our system only depend on one variable each, whereas predator-prey and epidemic models always have nonlinear terms which involve both variables. In this paper, we find complex behavior in a class of planar systems that is different from predator-prey models both biologically and mathematically.

The complex behavior only occurs in a small parameter region (see [34, Chapter 11] for a discussion of other parameter ranges). In this parameter region, the per capita mortality rate of juveniles is smaller than the one of adults ($\mu \leq 1 = \alpha$), and almost every juvenile makes it into the adult stage if there is no competition (the small values of m result in $p_0 \approx 1$). This would hold for species where the juveniles are less prone to enemies than the adults, and the juvenile stage is very short if there are plenty of resources available. We expect that the complex behavior can be observed in a larger parameter region if more sophisticated nonlinearities than the classical Ricker function are chosen to model the competition among juveniles and adults. A thorough understanding of the basic stage-structured model is important because its simplicity makes it a useful building block in models for several species. Recently it has been used (extended by an intermediate stage of subadult individuals) to explain emergent Allee effects in predators that feed on structured prey populations [9].

The results show that despite the low dimension of the system, the dependence of the resulting long-term dynamics on parameter values can be rather complex. The rich behavior of our model is caused by the interaction of intra-adult competition and intra-juvenile competition. None of the two alone can generate multiple positive attractors. It is essential that the intra-juvenile competition does not only affect juvenile mortality, but also juvenile maturation (the per capita transition rate). A

density-dependent per capita juvenile mortality rate alone, even if combined with a density-dependent per capita birth rate, can neither generate Hopf bifurcation nor multiple interior equilibria. This feature seems to be related to the fact that in our ODE model the length of the juvenile period is exponentially distributed. If the length of the juvenile period is the same for all individuals (at least for those that are born at the same time), then a density-dependent per capita birth rate can lead to periodic solutions without any other nonlinear model ingredients [21, 28].

Acknowledgments. B.W.K. would like to thank Martin Boer for valuable discussions.

REFERENCES

[1] A. D. Bazykin, *Nonlinear Dynamics of Interacting Populations*, World Scientific, Singapore, 1998.

[2] A. D. Bazykin, Yu. A. Kuznetsov, and A. I. Khibnik, in *Bifurcation Diagrams of Planar Dynamical Systems*, Ser. Math. Cybernetics, Research Computing Centre, USSR Academy of Sciences, Pushchino, Moscow Region, 1985 (in Russian).

[3] H. Caswell, *Matrix Population Models, Construction, Analysis, and Interpretation*. Sinauer Associates Inc., Sunderland, MA, 2001.

[4] A. R. Champneys and Yu. A. Kuznetsov, *Numerical detection and continuation of codimension-two homoclinic bifurcations*. Internat. J. Bifur. Chaos Appl. Sci. Engrg., 4 (1994), pp. 795–822.

[5] A. R. Champneys, Yu. A. Kuznetsov, and B. Sandstede, *A numerical toolbox for homoclinic bifurcation analysis*, Internat. J. Bifur. Chaos Appl. Sci. Engrg., 6 (1996), pp. 867–887.

[6] J. M. Cushing, *An Introduction to Structured Population Dynamics*, Volume 71, Society for Industrial and Applied Mathematics, Philadelphia, 1998.

[7] J. M. Cushing, R. F. Costantino, B. Dennis, R. A. Desharnais, and S. M. Henson, in *Chaos in Ecology: Experimental Nonlinear Dynamics*, Theoretical Ecology Series, Academic Press, San Diego, 2003.

[8] A. M. de Roos, *A gentle introduction to physiologically structured population models*, in Structured-Population Models in Marine, Terrestrial, and Freshwater Systems, S. Tuljapurkar and H. Caswell, eds., Chapman & Hall, New York, 1997, pp. 119–204.

[9] A. M. de Roos, L. Persson, and H. R. Thieme, *Emergent Allee effects in top predators feeding on structured prey populations*, Proc. Roy. Soc. Lond. Ser. B, 270 (2003), pp. 611–618.

[10] O. Diekmann, M. Gyllenberg, H. Huang, M. Kirkilionis, J. A. J. Metz, and H. R. Thieme, *On the formulation and analysis of general deterministic structured population models. II. Nonlinear theory*, J. Math. Biol., 43 (2001), pp. 157–189.

[11] E. J. Doedel, A. R. Champneys, T. F. Fairgrieve, Y. A. Kuznetsov, B. Sandstede, and X. Wang, *Auto 97: Continuation and bifurcation software for ordinary differential equations*, Technical report, Concordia University, Montreal, Canada, 1997.

[12] F. Dumortier, R. Roussarie, J. Sotomayor, and H. Żoladek, *Bifurcations of Planar Vector Fields. Nilpotent Singularities and Abelian Integrals*, Springer-Verlag, Berlin, 1991.

[13] E. Freire, L. Pizarro, A. J. Rodríguez-Luis, and F. Fernández-Sánchez, *Multiparametric bifurcations in an enzyme-catalyzed reaction model*, Internat. J. Bifur. Chaos Appl. Sci. Engrg., 15 (2005), pp. 905–947.

[14] E. Gamero, E. Freire, and E. Ponce, *On the normal forms for planar systems with nilpotent linear parts*, in Bifurcation and Chaos: Analysis, Algorithms, Applications, R. Seydel, F. W. Schneider, T. Küpper, and H. Troger, eds., Birkhäuser, Basel, Switzerland, 1991, pp. 123–127.

[15] W. Govaerts, Yu. A. Kuznetsov, and B. Sijnave, *Numerical methods for the generalized Hopf bifurcation*, SIAM J. Numer. Anal., 38 (2000), pp. 329–346.

[16] J. Guckenheimer and P. Holmes, in *Nonlinear Oscillations, Dynamical Systems and Bifurcations of Vector Fields*, 2nd ed., Appl. Math. Sci. 42, Springer-Verlag, New York, 1985.

[17] W. S. C. Gurney and R. M. Nisbet, *Ecological Dynamics*, Oxford University Press, New York, 1998.

[18] A. I. Khibnik, Yu. A. Kuznetsov, V. V. Levitin, and E. V. Nikolaev, *Continuation techniques and interactive software for bifurcation analysis of ODEs and iterated maps*, Phys. D, 62 (1993), pp. 360–371.

[19] E. Knobloch, *Normal forms for bifurcations at a double zero eigenvalue*, Phys. Lett. A, 115 (1986), pp. 199–201.
[20] B. W. Kooi and F. D. L. Kelpin, *Physiologically structured population dynamics, a modeling perspective*, Comments on Theoret. Biol., 8 (2003), pp. 125–168.
[21] T. Kostova, J. Li, and M. Friedman, *Two models for competition between age classes*, Math. Biosci., 157 (1999), pp. 65–89.
[22] Yu. A. Kuznetsov, in *Elements of Applied Bifurcation Theory*, 2nd ed., Appl. Math. Sci. 112, Springer-Verlag, New York, 1998.
[23] Yu. A. Kuznetsov, *Numerical normalization techniques from all codim 2 bifurcations of equilibria in ODE's*, SIAM J. Numer. Anal., 36 (1999), pp. 1104–1124.
[24] Yu. A. Kuznetsov, *Practical computation of normal forms on center manifolds at codim 3 Bogdanov–Takens bifurcations*, in preparation.
[25] Yu. A. Kuznetsov and V. V. Levitin, *CONTENT: Integrated environment for the analysis of dynamical systems*, version 1.5, Centrum voor Wiskunde en Informatica (CWI), Amsterdam, The Netherlands, 1997.
[26] V. I. Lukyanov, *Bifurcations of dynamical systems with a saddle-point separatrix loop*, Differential Equations, 18 (1982), pp. 1049–1059.
[27] J. A. J. Metz and O. Diekmann, in *The Dynamics of Physiologically Structured Populations*, Lect. Notes in Biomath. 68, Springer-Verlag, Berlin, 1986.
[28] R. M. Nisbet, *Delay-differential equations for structured populations*, in Structured-Population Models in Marine, Terrestrial, and Freshwater Systems, S. Tuljapurkar and H. Caswell, eds., New York, Chapman & Hall, 1997, pp. 89–118.
[29] V. P. Nozdracheva, *Bifurcation of structurally unstable separatrix loop*, Differentsial'nyye Uravneniya, 18 (1982), pp. 1551–1558.
[30] S. Ruan and W. Wang, *Dynamical behavior of an epidemic model with a nonlinear incidence rate*, J. Differential Equations, 188 (2003), pp. 135–163.
[31] M. Scheffer, S. Rinaldi, and Y. A. Kuznetsov, *Effects of fish on plankton dynamics: A theoretical analysis*, Canad. J. Fisheries and Aquatic Sci., 57 (2000), pp. 1208–1219.
[32] R. Seydel, *Practical Bifurcation and Stability Analysis-From Equilibrium to Chaos*, Springer-Verlag, New York, 1994.
[33] S. Tang and L. Chen, *Multiple attractors in stage-structured population models with birth pulses*, Bull. Math. Biol., 65 (2003), pp. 479–495.
[34] H. R. Thieme, *Mathematics in Population Biology*, Princeton University Press, Princeton, NJ, 2003.
[35] S. Tuljapurkar and H. Caswell, eds., *Structured Population Models in Marine, Freshwater, and Terrestrial Systems*, Chapman & Hall, New York, 1997.
[36] S. Wiggins, *Introduction to Applied Nonlinear Dynamical Systems and Chaos*, Texts Appl. Math. 2, Springer-Verlag, Berlin, 1990.
[37] E. P. Volokitin and S. A. Treskov *Qualitative analysis of a mathematical model for the reaction of catalytic oxidation*, in Mathematical Problems in Chemical Kinetics, Novosibirsk, pp. 149–175. K. I. Zamaraev and G. S. Yablonskii, eds., "Nauka" Sibirsk. Otdel, 1989, (in Russian).
[38] D. Xiao and S. Ruan, *Bogdanov-Takens bifurcations in predator-prey systems with constant harvesting*, in Differential Equations with Applications to Biology, S. Ruan, G. S. K. Wolkowitz, and J. Wu, eds., Fields Inst. Commun. 21, AMS, Providence, RI, 1999, pp. 493–506.
[39] D. Xiao and S. Ruan, *Codimension two bifurcations in a predator-prey system with group defense*, Internat. J. Bifur. Chaos Appl. Sci. Engrg., 11 (2001), pp. 2123–2131.
[40] H. Zhu, S. A. Campbell, and G. S. K. Wolkowicz, *Bifurcation analysis of a predator–prey system with nonmonotonic functional response*, SIAM J. Appl. Math., 63 (2002), pp. 636–682.